

The compressive response of ultra-high molecular weight polyethylene fibres and composites

J.P. Attwood^{*}, N.A. Fleck^{*}, H.N.G. Wadley[§] and V.S. Deshpande^{*1}

^{*}Department of Engineering, University of Cambridge, Trumpington Street, Cambridge, UK.

[§]Department of Material Science & Engineering, School of Engineering and Applied Science, University of Virginia, Charlottesville, VA 22904, USA.

Abstract

Measurements are reported for the compressive response of Ultra-high molecular weight polyethylene (UHMWPE) fibres and laminated composites loaded along the fibre direction. The compressive strength of the fibres was measured by both recoil tests and knot (or bend) tests. The strength of the fibres is governed by micro-kinking of the fibrils within the fibres. The recoil tests suggest that this kinking occurs at a compressive stress of approximately 340 MPa. Consistent with observations of other fibres such as Kevlar and carbon fibres, the compressive strength inferred from bending tests is approximately a factor of two higher than that from a direct compression test, such as the recoil test. The in-plane compressive response of laminated UHMWPE composites was measured using notched specimens. Two grades of composites with shear strengths of about 1.5 and 0.5 MPa were investigated and found to have compressive strengths of about 12 MPa and 3 MPa, respectively. Thus, unlike Kevlar composites, the composite compressive strength is not governed by the compressive strength of the fibres but by the micro-buckling of the composite plies. Detailed experimental measurements are reported for the kink-band width, fibre rotation within the band and its subsequent broadening after lock-up due to fibre rotation. These are shown to be adequately modelled by traditional kinking theory while a net section stress analysis models the propagation of the micro-buckle with sufficient fidelity.

Keywords: micro-buckling, kink-band, UHMWPE fibres, fibre crushing.

¹ Corresponding author: vsd@eng.cam.ac.uk

1. Introduction

Composites comprising ultra-high molecular weight polyethylene (UHMWPE) fibres in a polyurethane matrix were originally developed for personnel and vehicle armours because of their exceptionally high tensile strength to density ratio, but are now being evaluated for air cargo containers, as backing materials for solar panels, and radomes due to their microwave transparency. In most of these applications the composites are laminates comprising of unidirectional plies stacked in alternating 0° and 90° orientations.

Ultra-high molecular weight polyethylene fibres were commercialised in the late 1970s by DSM[®] under the trade name Dyneema[®], and more recently by Honeywell in the USA under the name Spectra[®]. The fibres are composed of many sub- μm diameter filaments each consisting of densely packed, extended chain polyethylene molecules with molecular weights exceeding 10^6Da . The fibres are highly anisotropic with properties in the fibre's longitudinal direction governed by the very strong $\text{sp}^3\text{C-C}$ bond while those in the radial direction are governed by weak van der Waals interactions. The fibres can be combined with thermoplastic polymers to make composite materials that can be shaped and consolidated by hot pressing below the melting point of the fibres ($\sim 135^\circ\text{C}$). A number of studies have been conducted to measure the static stress-strain response (Wilding & Ward 1978; Govaert & Lenstra 1992) and dynamic stress-strain response (Russell et al. 2013; O'Masta et al. 2014; Koh et al. 2010; Chocron Benloulou et al. 1997) of UHMWPE fibres and their composites. For example, Russell et al. (2013) have observed that UHMWPE composites have tensile strengths of a few GPa but shear strengths of only a few MPa. Moreover, they found that the tensile strength of UHMWPE fibres exhibits nearly no strain rate dependence for strain rates between 10^{-1} and 10^3 s^{-1} . Such measurements can provide the required inputs for continuum models (Grujicic et al. 2009; Iannucci & Pope 2011) with the eventual goal of predicting the penetration resistance of UHMWPE composites.

These studies all focused on the tensile and shear properties of UHMWPE composites. To respond to the emerging structural applications of these materials, knowledge of the compressive response of both the fibres and laminates is imperative. However, there is a paucity of measurements and models for the compressive response of UHMWPE in the literature. Notable exceptions are: (i) the work of Liu et al. (2013) who investigated the bending response of Dyneema[®] composite beams and observed the formation of a compressive kink-band on the compressive face of the beam and (ii) the studies by Attwood et al. (2014) and O'Masta et al. (2015) who investigated the out-of-plane compressive response of Dyneema[®] composites. However, there are no reported studies on the direct compressive response of Dyneema[®] fibres and composites along the fibre direction.

The main competing mechanisms governing the compressive strength of long fibre composites are: (i) elastic micro-buckling, which is an elastic instability involving matrix shear; (ii) plastic micro-buckling in which the matrix deforms plastically; (iii) fibre crushing due to compressive fibre failure; (iv) splitting by matrix cracking parallel to the main fibre direction; (v) buckle delamination and (vi) shear band formation at 45° to the main axis of loading due to matrix yielding, as reviewed by Fleck (1997). In composites with high toughness matrices, the micro-buckling and fibre crushing modes are most commonly encountered. For example, the compressive

strength of glass and carbon fibre polymer reinforced composites (GFRP and CFRP, respectively) is usually governed by elastic or plastic micro-buckling. While the micro-buckling strength is typically set by matrix properties, Kyriakides & Ruff (1997) showed that the wavelength, amplitude and distribution of imperfections and fibre waviness also strongly the strength of long-fibre composites. Moreover, Vogler & Kyriakides (1997) demonstrated that CFRP and GFRP composites can continue to carry (a reduced) load after the onset of micro-buckling by the broadening of the micro-buckle band. On the other hand, aramid fibre composites such as Kevlar typically fail by fibre crushing under compressive loading. In fact, Kevlar fibres themselves are micro-composites comprising wavy fibrils in a soft matrix and hence kink/crush by micro-buckling within the fibres, as shown by Greenwood & Rose (1974).

In this study we investigate some fundamental aspects of the in-plane compressive failure of Dyneema[®] composites. The outline of the paper is as follows. First, we report measurements of the compressive strength of Dyneema[®] fibres via both recoil and knot (bend) tests. Next, the compressive response of two grades of Dyneema[®] composites (with different polymer matrices but the same fibre) is investigated using an edge notched compression specimen. Measurements are reported for the propagation of the micro-buckle as well as the structure of the kink-band. Compressive strength predictions based on kinking theory are finally compared with the observations.

2. Compressive strength of fibres

When the matrix of a composite is sufficiently stiff and strong the usual elastic and plastic micro-buckling compressive failure mechanisms are not operative, and alternative failure modes such as fibre crushing intervene. Fibre crushing occurs when the uniaxial strain in the composite is equal to the intrinsic crushing strain ε_f^c of the fibres. A variety of mechanisms may be associated with fibre crushing including: (i) local crushing due to plastic yielding (e.g. in steel fibres) (Piggott & Wilde 1980; Fleck 1997); (ii) longitudinal splitting of glass fibres, and (iii) microscopic micro-buckling or kinking within each Kevlar or carbon fibre wherein the micro-fibrils within the fibres kink due to the deformation of the intervening matrix. Typical fibre crushing strains are $\varepsilon_f^c = 0.5$ and 2.5% for Kevlar and PAN-based carbon fibres, respectively. There are no reported fibre compressive strength measurements for ultra-high molecular weight polyethylene fibres and here we report compressive strength measurements for single SK76² fibres using two techniques. Measurements of its other mechanical properties can be found in (Russell et al. 2013).

2.1 Recoil tests

Allen (1987) developed a recoil technique to measure fibre compressive strengths. Here we summarize salient aspects of this technique, and refer readers to (Allen 1987) for further details. A single filament/fibre is rigidly clamped at one end and a known weight W hung vertically from the other (Fig. 1a). Under static conditions this generates a tensile stress

² SK76 is a grade of the Dyneema[®] UHMWPE fibre manufactured by DSM.

$$\sigma_0 = \frac{W}{\pi a^2} \quad (2.1)$$

within the fibre, where a is the radius of the circular fibre. This fibre is then suddenly cut at a length L_0 from the rigid support at time $t = 0$. The spatio-temporal evolution of the stress within the fibre, assuming that the fibre remains linear elastic, is sketched in Fig. 1b with $x = 0$ and $x = L_0$ corresponding to the clamped and cut edges of the fibre. At time $t = 0^-$, the stress $\sigma = \sigma_0$ throughout the fibre and reduces to zero at $x = L_0$ at $t = 0$. This zero stress front then moves from $x = L_0$ towards the clamped end as the initial tensile strain energy is converted to kinetic energy with the fibre material acquiring a velocity $v_0 = \sigma_0/\sqrt{E\rho}$, where E and ρ are the Young's modulus and density, respectively of the fibre. At time $t = L_0/c$, where $c = \sqrt{E/\rho}$ is the longitudinal elastic wave speed, the release stress wave reaches the clamped end, and the fibre becomes stress free, but is being driven at velocity v_0 towards the clamped end. The clamp, however, forms a rigid boundary and the fibre's kinetic energy is converted back into strain energy as a compressive stress of magnitude σ_0 begins to propagate down the fibre at a wave speed, c . If no dissipation (dampening or damage) occurs, this wave propagation sequence continues, and the axial stress in the fibre oscillates between tension and compression.

This solution shows that the magnitude of the compressive stress wave generated during recoil is equal in magnitude to the initial imposed tensile stress. The compressive strength of fibres due to fibre kinking is usually significantly less than their tensile strength. Thus, an initial tensile stress can be used to generate a compressive stress over a small segment of the fibre (small enough to avoid triggering macroscopic buckling) and hence measure the kinking or crushing strength of the fibre. Unfortunately, this analysis does not give the number of kinks formed during the recoil, or their spacing, without knowledge of the dissipation during the kinking process. However, the critical initial tensile stress at which kinking is first observed gives the compressive failure strength for the fibres.

The analysis outlined above indicates that compressive damage/kinking due to the recoil will first occur near the clamped end of the fibre. As compressive damage develops, the associated dissipation will reduce the intensity of the compressive stress wave away from the clamped end. Thus, with decreasing σ_0 kinks will form nearer and nearer the clamped end until a critical value of σ_0 is reached below which no kinks will be observed. This critical value of σ_0 is labelled as the compressive strength σ_c of the fibres.

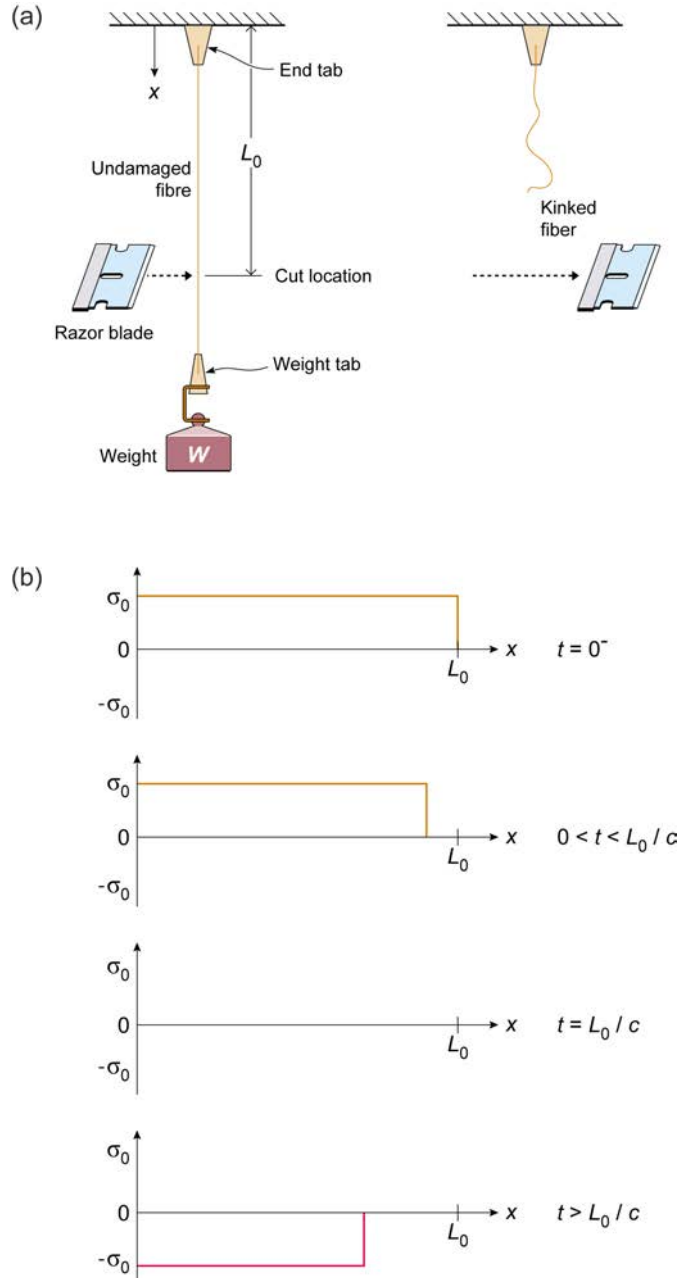


Figure 1: Sketches of (a) the setup used to measure the fibre compressive strength via the recoil test and (b) the spatio-temporal evolution of the stress state within the fibre after release of the weight at time $t = 0$.

The experiments were conducted as follows. The weight W was hung from the fibre to create a tensile force. After the system stabilized and was at rest, the fibre was cut with one quick stroke of a sharp razor blade at a length $L_0 = 40$ mm from the clamped end. The clamped end of the fibre was then viewed under an optical microscope to observe whether a kink had formed and the process repeated with a larger W until a kink was observed. In the experiments performed in this study, W was increased so that the tensile force applied to the fibre was raised from an initial value of 20 mN in increments of 10 mN. No kinks were observed for $W \leq 80$ mN but extensive kinking was observed for $W = 90$ mN. The experiments were then repeated for the range $80 \text{ mN} \leq W \leq 90 \text{ mN}$ in increments of 1 mN. A sequence of scanning-electron micrographs of the SK76 fibre near its clamped ends are shown in Fig. 2 for four selected values of $W = 85$ mN, 86 mN, 87 mN and 88 mN. Clearly, no kinks are

observed for $W = 85$ mN and only a faint kink was observed for $W = 86$ mN (highlighted by a circle in Fig. 2b). A much more distinct single kink is seen at $W = 87$ mN while multiple kinks are observed at $W = 88$ mN. We thus argue that kinking initiates in the SK76 fibres at $W = 86$ mN. The fibre radius $a \approx 9$ μm which via Eq. (2.1) translates to a compressive kinking stress of $\sigma_c \approx 340$ MPa. Multiple repeat measurements confirmed that the scatter in this measured value is no more than $\pm 1\%$.

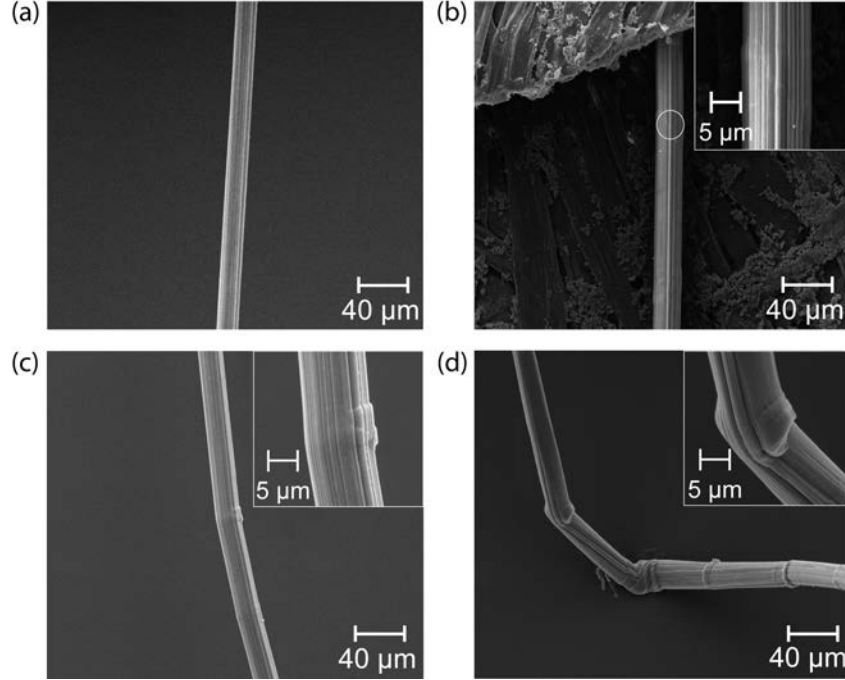


Figure 2: Post recoil test SEM micrographs of the SK76 fibre showing sections near the clamped end. The micrographs are shown for selected values of the force applied by the weight W : (a) 85 mN (no kinks); (b) 86 mN (faint kink highlighted by the white circle and shown at higher magnification in the inset); (c) 87 mN (a clear single kink) and (d) 88 mN (multiple kinks).

2.2 Knots tests

A knot test as proposed by Jones & Johnson (1971) was also performed in order to obtain an independent estimate of the compressive strength. In this test, a single SK76 fibre was tied into a loose knot with an approximately circular loop as sketched in Fig. 3. The two loose ends of the fibre were clamped and then one end pulled using a sliding mechanism driven by a stepper motor within a scanning electron microscope (SEM) as illustrated in Fig. 3. This pulling action reduces the radius of the loop and simple bending theory dictates that the magnitude of maximum compressive strain on the compressive side of the loop with a local radius of curvature R is given by $\varepsilon_{max} = a/R$. Thus, with decreasing R the induced compressive strain increases and at a critical value $\varepsilon_{max} = \varepsilon_c$ we anticipate a kink to be introduced within the fibre.

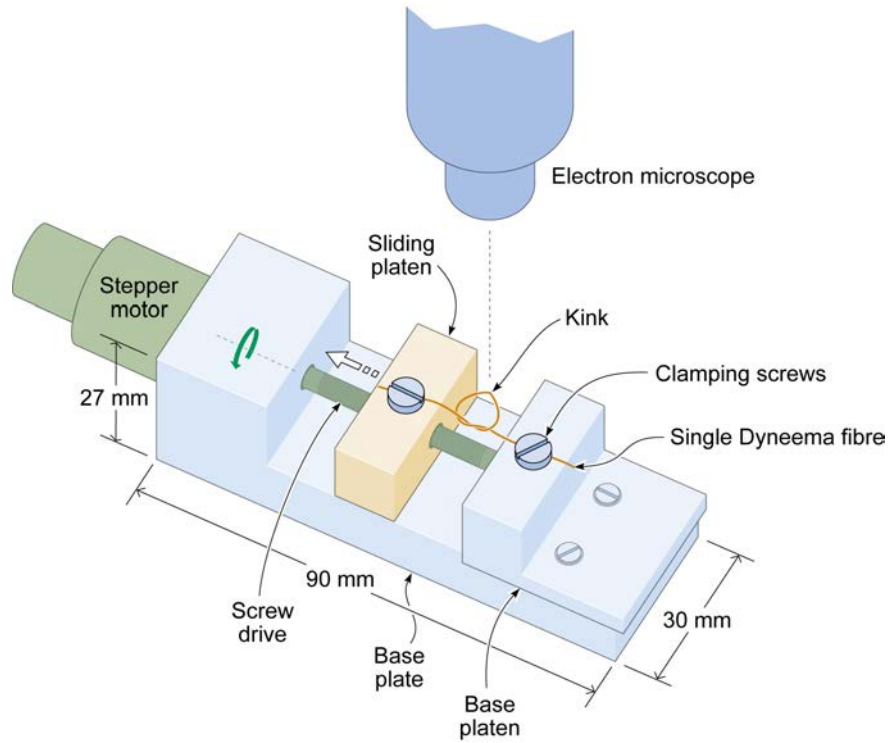


Figure 3: Sketch of the apparatus used to perform the knot test in situ within a SEM.

These knot tests were carried out in the SEM with an initial value of $R = 1.031$ mm (Fig. 4a) and R was then decreased in increments of 0.1 mm. At each increment the entire knot was scanned to observe the development of kinks. If no kinks were observed then the next loading increment was made. When the first kink was observed in the loop the local radius of curvature of the fibre in the vicinity of the kink was $R = 0.845$ mm. A sequence of SEM images with increasing magnification is shown in Figs. 4b through 4d to show the location of the kink and the measurement of R . Moreover, in Fig. 4d we clearly see that the kink is well formed on the inner (compressive) side of the loop but does not fully propagate through the entire cross-section of the fibre as the outer side is under tensile strain. The kinking strain is then estimated as $\varepsilon_c \approx 1.07\%$ using the values $a \approx 9$ μm and $R = 0.845$ mm.

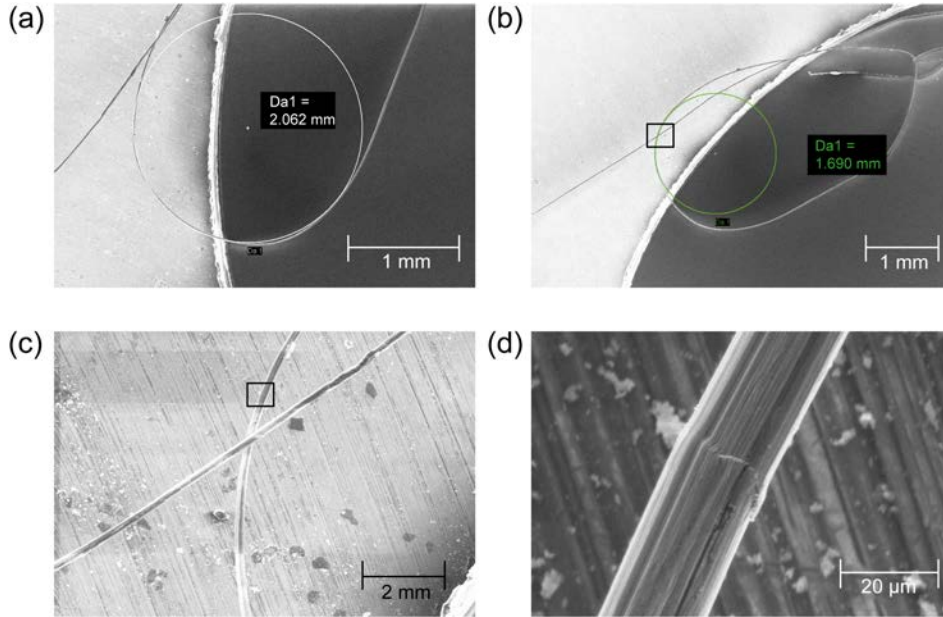


Figure 4: SEM micrographs of the knot test on the SK76 fibre. (a) The initial knot with a radius $R = 1.031$ mm. (b) Image of the entire knot at the initiation of damage with $R = 0.845$ mm. (c) Magnified view of the kink site in (b) and (d) magnified image of the kink in (b).

The Young's modulus of the SK76 fibres under quasi-static strain rates of 10^{-3}s^{-1} was measured by (Russell et al. 2013) to be $E_f = 82$ GPa. The compressive failure/kinking strength as estimated from this knot test is then given by $\sigma_c = E_f \varepsilon_c \approx 877$ MPa. This value is approximately 2.5 times the compressive strength obtained from the recoil tests. This is consistent with observations of aramid fibres (Greenwood & Rose 1974) in which bend tests typically give compressive strengths between 2-3 times higher compared to those obtained from composite compression tests. This is most likely due to the fact that the strain gradients imposed in the bend test stabilise the micro-buckling of the fibrils compared with the uniform stress state present in composite compression or recoil tests³.

3. Compressive response of composites

The in-plane compressive response of fibre composites has received significant attention with the main focus being on carbon or glass fibre reinforced polymer composites (CFRP or GFRP) and, to a lesser extent, Kevlar composites. There is broad consensus that the in-plane compressive strength (for loading along the fibre direction) of most CFRP and GFRP composites is governed by a micro-buckling phenomena involving (elastic or plastic) shearing of the matrix. Consider a unidirectional composite with an infinitely long band of width w within which the fibres are misaligned at an initial angle $\bar{\phi}$ as shown in Fig. 5a. This band of imperfection is inclined at an angle $\pi/2 - \beta$ with respect to the remote fibre direction. Neglecting the bending resistance of the fibres, Budiansky (1983) showed that the compressive strength of the composite for $\beta = 0$ is given as

³ Some preliminary tests under an optical microscope confirmed that the SEM environment did not significantly affect the behaviour of the SK76 fibre in the knot test.

$$\sigma_{mb} = \frac{G}{1 + \bar{\phi}/\gamma_Y} \quad (3.1)$$

where G and γ_Y are the shear modulus and shear yield strains, respectively, of the matrix material. Thus, the compressive strength of CFRP and GFRP composites is typically independent of the compressive failure strength of the individual fibres. On the other hand, the compressive kinking/failure strength of Kevlar composites is typically low, with a failure strain $\varepsilon_c \approx 0.5\%$. Thus, compressive failure occurs by fibre crushing and is given for a unidirectional composite with fibre volume fraction V_f by a rule of mixtures formula as

$$\sigma_{crush} = [V_f E_f + (1 - V_f) E_m] \varepsilon_c, \quad (3.2)$$

where E_f and E_m are the Young's moduli of the fibre and matrix, respectively. Other compressive failure modes of unidirectional composites include splitting and buckle delamination. These modes typically occur in composites with low toughness matrices.

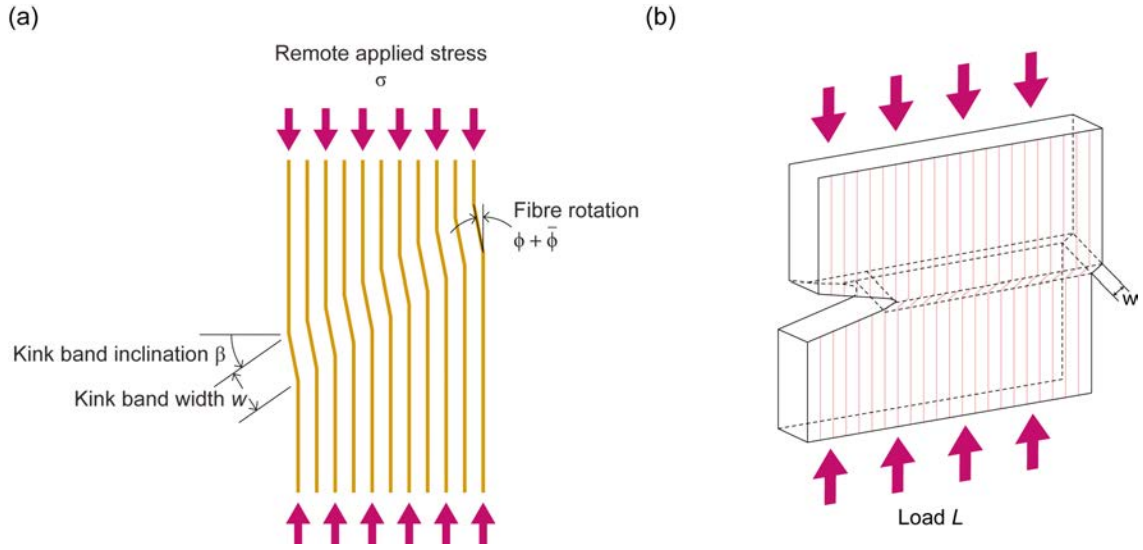


Figure 5: (a) Schematic of out-of-plane micro-buckling in a unidirectional composite under compressive loading. The fibre misalignment angle, kink band inclination, kink band width and remote stress are indicated on the sketch. (b) A 3D sketch of the micro-buckle emanating from the notch root and having traversed through the specimen width.

3.1 Materials

The aim here is to measure the compressive response of composites comprising ultra-high molecular weight polyethylene fibres and develop an understanding of their compressive deformation/failure modes. We consider here two grades of Dyneema[®] composites manufactured by DSM[®] with commercial designations HB26 and HB50. Both composites are laminates comprising alternating 0° and 90° plies of thickness $t = 60 \mu\text{m}$ and SK76 fibres with a volume fraction of 83%; see sketch in Fig. 6a. The difference between the two composites lies in the polyurethane matrix material. While

the HB26 composite contains a polyetherdiol-aliphatic diisocyanate polyurethane (PADP) matrix the HB50 composite uses a weaker styrene-isoprene-styrene tri-block copolymer (SISTC) matrix. Dark field optical micro-graphs of the cross-sections through the HB26 and HB50 composites are included in Figs. 6b and 6c respectively, to show the ply arrangements and thicknesses while in Fig. 6d a micrograph of the HB26 composite is included to show a magnified view of the ply and fibres: from this and similar images we estimate the initial waviness of the plies to be $\bar{\phi} \approx 4^\circ$.

In-plane tensile tests of the $[0^\circ/90^\circ]$ HB26 and HB50 composites conducted at an applied strain of 10^{-3}s^{-1} reported in Russell et al. (2013) show that the tensile response of both these composites are nearly indistinguishable and can be approximated as elastic-brittle. The measured tensile Young's modulus and tensile strength of both composite grades are $E = 34 \text{ GPa}$ and $\sigma_T = 800 \text{ MPa}$, respectively. On the other hand, interlaminar shear tests for these two composites grades was markedly different with peak shear strengths of $\tau_Y = 1.8 \text{ MPa}$ and 0.2 MPa for the HB26 and HB50 composites, respectively. For the sake of completeness these measurements are detailed in Appendix A.

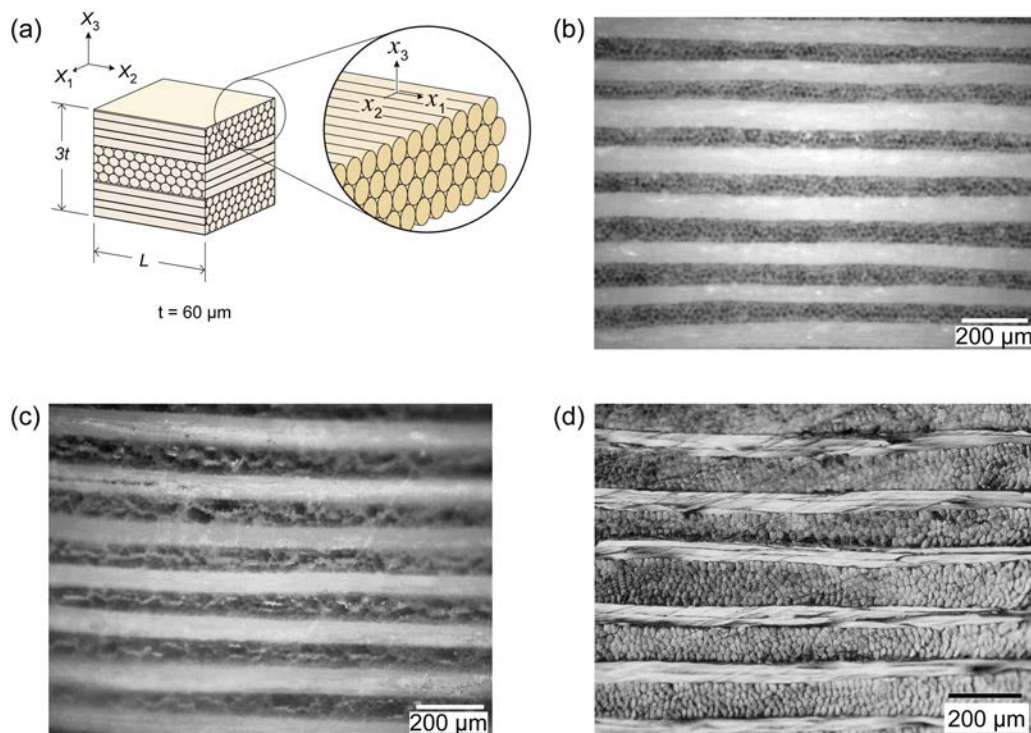


Figure 6: (a) A three-dimensional sketch showing the ply arrangements of the $[0^\circ/90^\circ]$ Dyneema® composite. Dark field microscopy images of the (b) HB26 and (c) HB50 composite grades and (d) an optical micrograph showing a magnified view of the plies and fibres in the HB26 composite. The initial ply waviness is inferred to be $\bar{\phi} \approx 4^\circ$ from this SEM image.

3.2 Experimental protocol for compression tests

Compression tests on edge-notched specimens were conducted using two geometrically self-similar specimen geometries labelled type A and B. The bulk of the tests on the HB26 composite were carried out using the larger type A while a limited number of tests were performed on the HB26 and HB50 composites using the smaller type B. All dimensions of specimen type B were a factor of 3.3 smaller compared to the type A specimens.

The geometry of specimen type A is sketched in Fig. 7 with the inset illustrating the fibre/ply orientations with respect to the specimen. Rectangular specimens of height $H = 200$ mm, width $D = 117$ mm and thickness $b = 20$ mm were cut from sheets of the Dyneema[®] composite supplied by DSM. An edge notch of depth $d = 33.3$ mm and root radius $r = 3.35$ mm was machined in these plates as shown such that the opening at the mouth of the notch was 20 mm. The root of the notch was then sliced with a sharp razor blade to give a repeatable root stress concentration. The specimen was tightly clamped at both ends in nylon holders as sketched in Fig. 7 so that the free height of the specimen was 267 mm. These holders prevented brooming of the specimen at the ends where the compression loads were applied. A clip gauge with a gauge length of 30 mm was attached 20 mm ahead of the root of the notch with the two arms of the gauge located equi-distant from the mid-plane of the plate. The specimen was compressed between rigid loading platens of a screw driven test machine at an applied displacement rate of 1.7 mm/min with the applied load L measured from the load cell of the test machine and the applied remote stress then defined as

$$\sigma \equiv \frac{L}{b(D - d)}. \quad (3.3)$$

It will be shown later that micro-buckles initiate at the root of the notch and propagate along the width of the specimen. To aid measurement of the micro-buckle length, vertical lines at 2 mm intervals were marked on the face of the specimen ahead of the notch. The progression of the micro-buckle was then monitored by taking a series of images of the front face (Fig. 8a-d) and the un-notched edge (Fig. 9 a-d) of the specimen at intervals of 1s during the deformation using a CCD Colour Microscopy PixeLINK[®] camera⁴.

⁴ The camera used a 1:1.4/25 mm lens and digital images with a resolution of 2048 x 1536 pixels were captured.

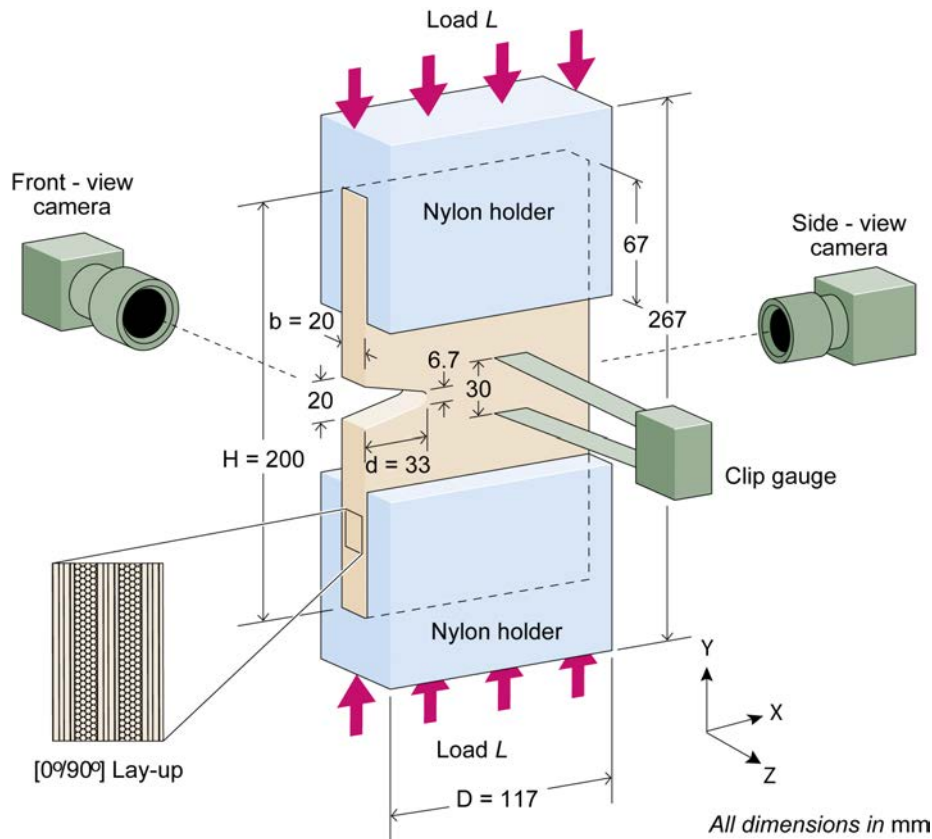


Figure 7: Sketch showing the geometry of specimen type A. The sketch includes the clip gauge used to measure the applied displacement, δ and the inset shows the ply arrangements in the side view. All dimensions are labelled in mm.

Additional high-resolution SEM images of the micro-buckle were also taken in order to visualise the damage to the fibres in more detail. Conventional polishing techniques cannot be used to prepare Dyneema[®] for SEM imaging as the relatively low transverse hardness of the fibres results in extensive shear deformation during polishing. Samples were first trimmed to an appropriate size for imaging. Face-imaged samples were prepared by peeling away the outer plies, then removing the excess matrix material with a sharp blade. Edge-imaged samples were sliced with a sharp razor blade to reveal a smooth edge surface. These samples were then sputter coated with gold prior to imaging in the SEM.

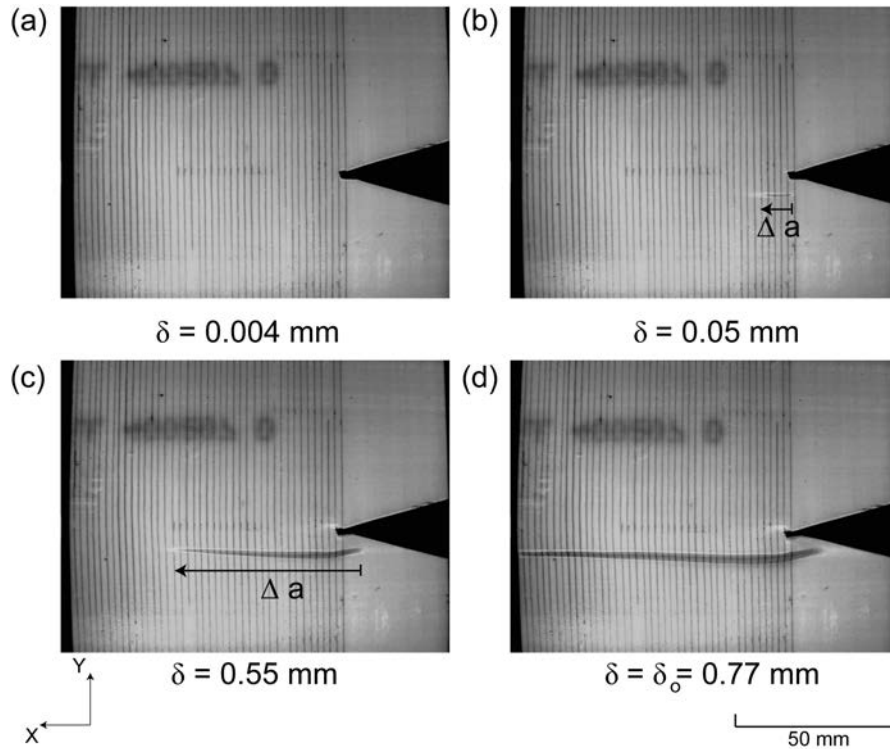


Figure 8: A montage of images of the front of the specimen showing the progression of the micro-buckle across the HB26 type A specimen. Images are shown at selected values of the applied displacement, δ , and the micro-buckle propagation Δa is labelled in (b) and (c). Note that on the side of the specimen shown in these photographs the out-of-plane micro-buckle is below the notch root but aligned with the notch root on the other side of the specimen.

3.3 Compressive response of the HB26 composite

Unless otherwise mentioned, we report the compressive response of the HB26 composite measured using specimen type A. The measured applied compressive stress σ versus the displacement δ measured by the clip gauge for a type A specimen is plotted in Fig. 10a. After an initially elastic response, a peak stress is attained at $\sigma = \sigma_{\max} \approx 12$ MPa at $\delta \approx 0.025$ mm with a subsequent softening response. The experiments were terminated at $\delta = 5$ mm when the out-of-plane displacement of the specimen due to micro-buckling (discussed subsequently) exceeded 10% of the specimen thickness. This out-of-plane deformation induced very large bending stresses and renders the measurement no longer appropriate for the compressive response under discussion here.

Photographs of the front of the specimen (view sketched in Fig. 7a) are shown at selected values of δ in Fig. 8. A micro-buckle is seen to initiate at the root of the notch near to the point when the peak stress in Fig. 10a is attained. Subsequently, this micro-buckle propagates approximately horizontally from the notch root towards the left edge of the specimen in Fig. 8d. The images in Fig. 8 suggest that the micro-buckle broadens in its wake as it propagates, i.e. the width of the micro-buckle is larger near the notch root compared to at its tip. The structure and broadening of the micro-buckle shall be made explicit subsequently.

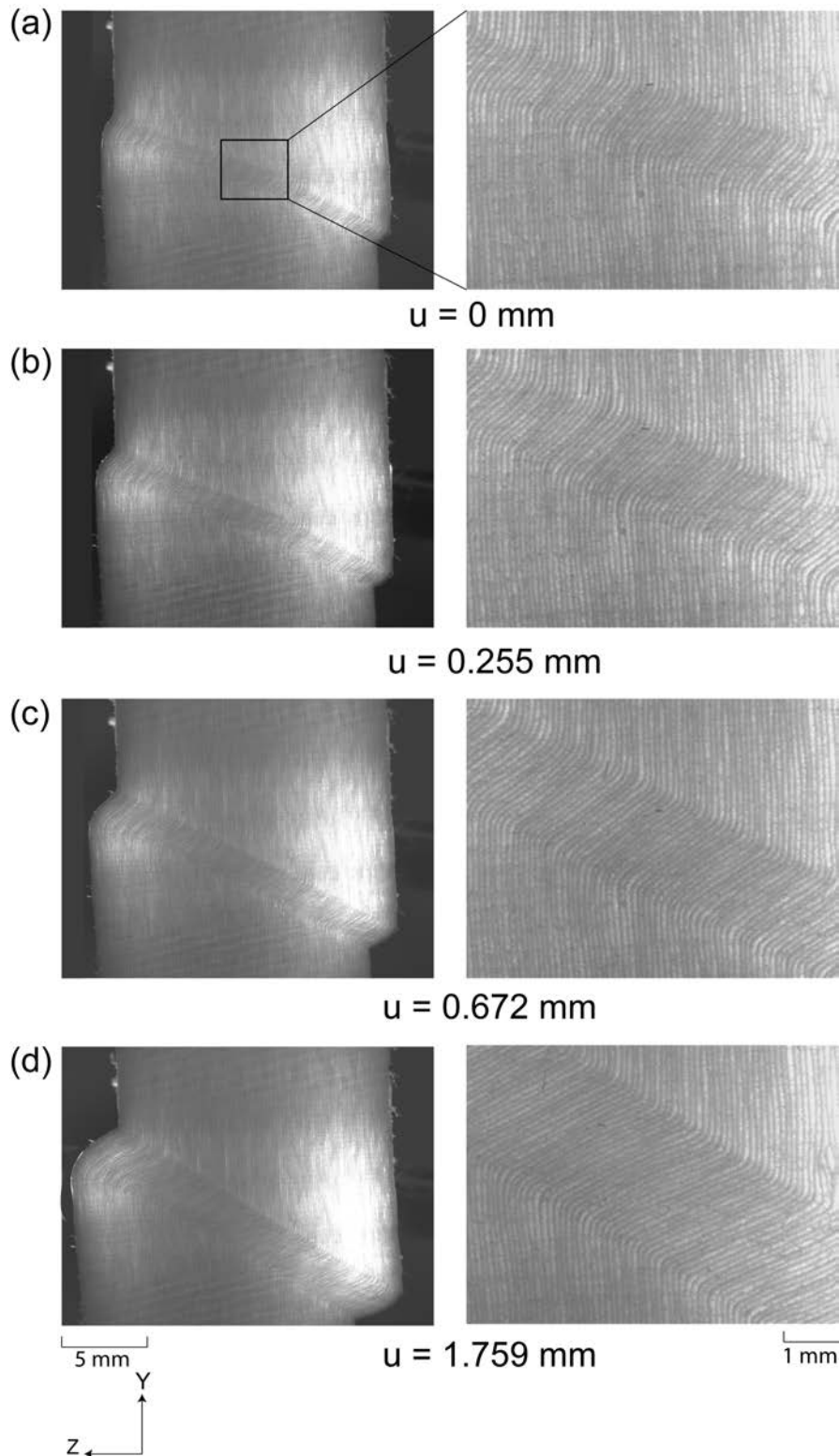


Figure 9: A montage of images viewed with the side camera showing the development of the kink band in the type A HB26 specimen. Images are shown at selected values of the displacement, u . (a) and (b) show a kink band of fixed width with increasing fibre rotation and (c) and (d) a kink band with fixed fibre rotation and increasing width.

To characterize the micro-buckle, define Δa as the distance the micro-buckle has propagated at any instant in the deformation. The applied remote stress σ versus Δa relation inferred from the photographs of the front of the specimen is included in

Fig. 10b. This confirms that micro-buckle propagation begins at $\sigma = \sigma_{\max} \approx 12$ MPa and the applied stress σ then decreases with increasing Δa . This is contrary to measurements of micro-buckle propagation in CFRP composites where σ first increases with increasing Δa and then reaches a plateau stress; see for example Sivashanker et al. (1996).

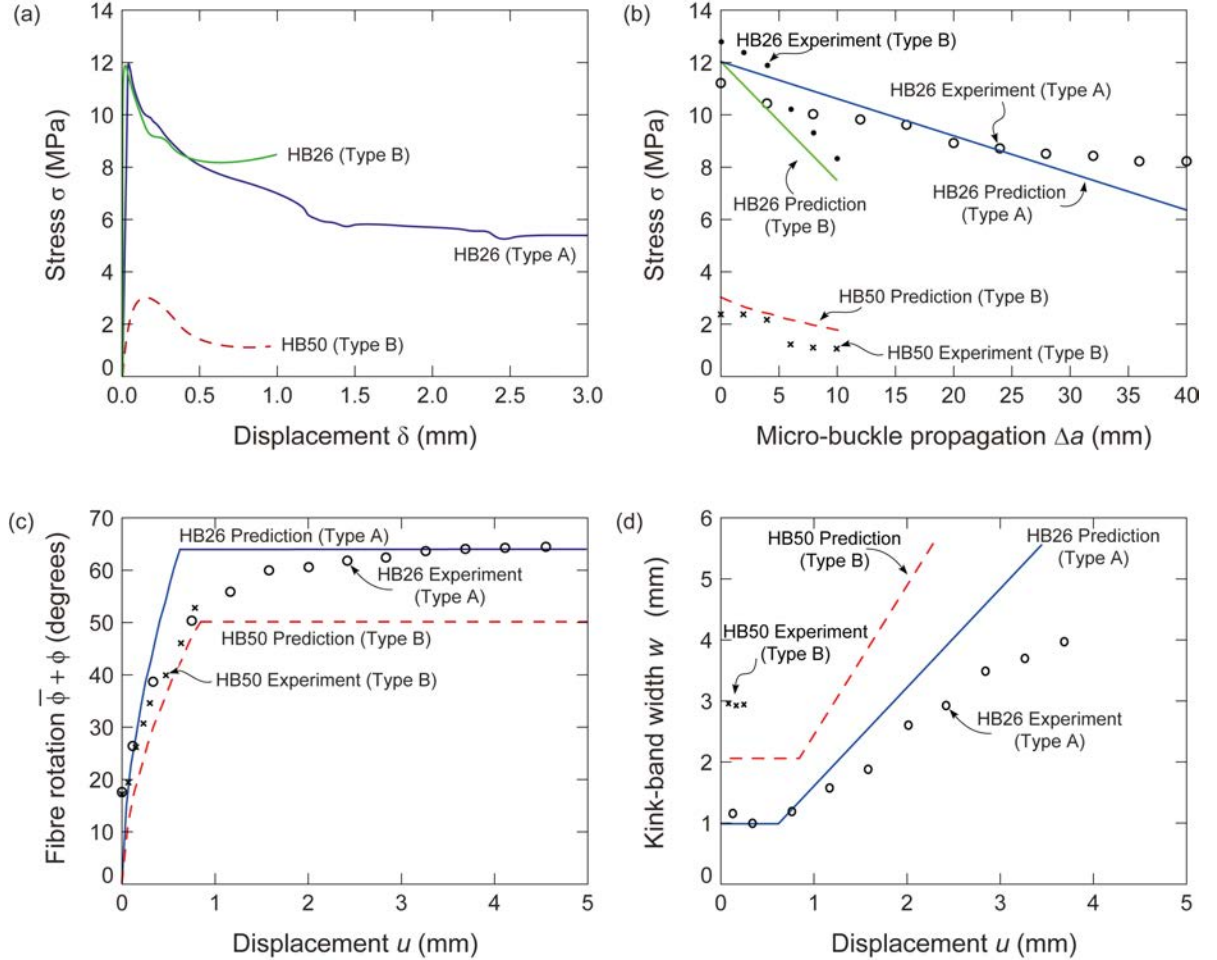


Figure 10: Measurements of (a) the remote stress σ versus applied displacement, δ ; (b) the remote stress σ versus micro-buckle propagation distance Δa ; (c) fibre rotation $\phi + \bar{\phi}$ versus displacement u and (d) kink-band width w versus displacement u for the HB26 and HB50 composites. In (a) and (b) data is included for both specimens type A and B while in (c) and (d) only data for specimen type A of the HB26 composite is shown. All data for the HB50 composite is for specimen type B. Predictions are also included in (b)-(d).

3.3.1 Structure of the micro-buckle

The micro-buckle reaches the left end of the specimen at an applied displacement $\delta_o = \delta = 0.77$ mm and from that instant onwards the evolution of the micro-buckle can be observed from the photographs using the side-view camera. Selected images from these photographs are included in Fig. 9 as the applied displacement, $u = \delta - \delta_o$ (the increment of applied displacement after the micro-buckle reaches the edge of the specimen) is increased. The images are shown at two levels of magnification: in column one the overall micro-buckle across the entire thickness $b = 20$ mm is shown while in column two, a magnified view of a central portion (marked in column one) is included to better illustrate the deformation within the micro-buckle. A clear micro-buckle band very similar to the sketch in Fig. 5a is seen at $u = 0$ mm in Fig. 9a. This

band is inclined at an angle $\beta = 36^\circ$ (the measured kink angle β falls within the range bounded by the short and long wavelength imperfection limits analysed by Budiansky (1983)) and with a width $w = 0.96$ mm. The misalignment angle $\bar{\phi} + \phi$ increases from Fig. 9a to 9b with increasing u while w remains approximately constant. However, after a critical value of misalignment is attained the misalignment angle remains constant at about $\bar{\phi} + \phi \approx 60^\circ$, and the band width w increases with increasing u , i.e. band broadening occurs as seen in Figs. 9c and 9d.

It is clear from the images in Figs. 8 and 9 that the micro-buckle in the HB26 composite is an out-of-plane micro-buckle similar to that reported extensively in CFRP composites (Sivashanker et al. 1996) and sketched in Fig. 5b. However, unlike those composites, the micro-buckles here occur due to interlaminar shear between the plies (rather than shearing between individual fibres). To clarify this, we include in Fig. 11 images at various magnifications of the micro-buckle as observed at the specimen edge at a displacement $u = 0.34$ mm. At this displacement, the micro-buckle at the specimen edge is still in the fibre rotation regime. Note that while the 0° and 90° plies are in fact approximately the same thickness (as shown in Fig. 6) the out-of-plane fibres have been smeared by cutting, making these plies appear thicker. It is clear from these images that: (i) the micro-buckle is occurring at the individual ply length scale with shearing and gaps opening up between the plies (visible in Fig. 11b-d as dark gaps between sections) but negligible deformation within the plies and (ii) no compressive kinks are observed in the fibres within the micro-buckled band, but rather there are kinks in the fibres at the edge of the band where the fibres are subjected to large curvatures.

Recall that the kinking stress of the fibres is around 340 MPa and thus based on the rule of mixtures (assuming negligible contribution to the compressive strength from the matrix and that the strength is set by compressive fibre kinking) the compressive strength of the HB26 composite is expected to be $(\sigma_c V_f)/2 = 141$ MPa. This is significantly higher than the measured value of 12 MPa. On the other hand, the micro-buckling strength given by Eq. (3.1) is approximately 18 MPa using the measured shear modulus $G = 60$ MPa (Liu et al. 2013), shear strength $\tau_Y = 1.8$ MPa and an initial misalignment angle $\bar{\phi} = 4^\circ$. This is in good agreement with the measured value of σ_{\max} . Based on the observations of Fig. 11 and the predictions of the micro-buckling strength, it is argued that the compressive strength of the HB26 composite is set by “ply” micro-buckling.

The observation that kinks occur in the fibres at the edge of the band gives an indication of the phenomena setting the micro-buckle width w . In an early study Budiansky (1983) gave an analysis of the band width w in a unidirectional composite based on the simplifying assumptions of perfectly straight fibres and rigid-ideally plastic behaviour of the composite in shear and transverse tension. In that analysis he included the couple stresses provided by fibre bending and calculated w by assuming that the band width is set by the strain at which the fibres break in tension. Here we can re-interpret the analysis as follows. Instead of the band width being set by fibre fracture, as in Budiansky’s study, the width is set by the kinking of the fibres in compression. In the limit of the fibre kinking strain $\varepsilon_c = 0$, the modified Budiansky analysis gives a simple closed-form expression for the band width w^* (prior to band broadening) as

$$\frac{w^*}{t} = \frac{\pi}{4} \left(\frac{E}{2\tau_Y} \right)^{1/3}. \quad (3.4)$$

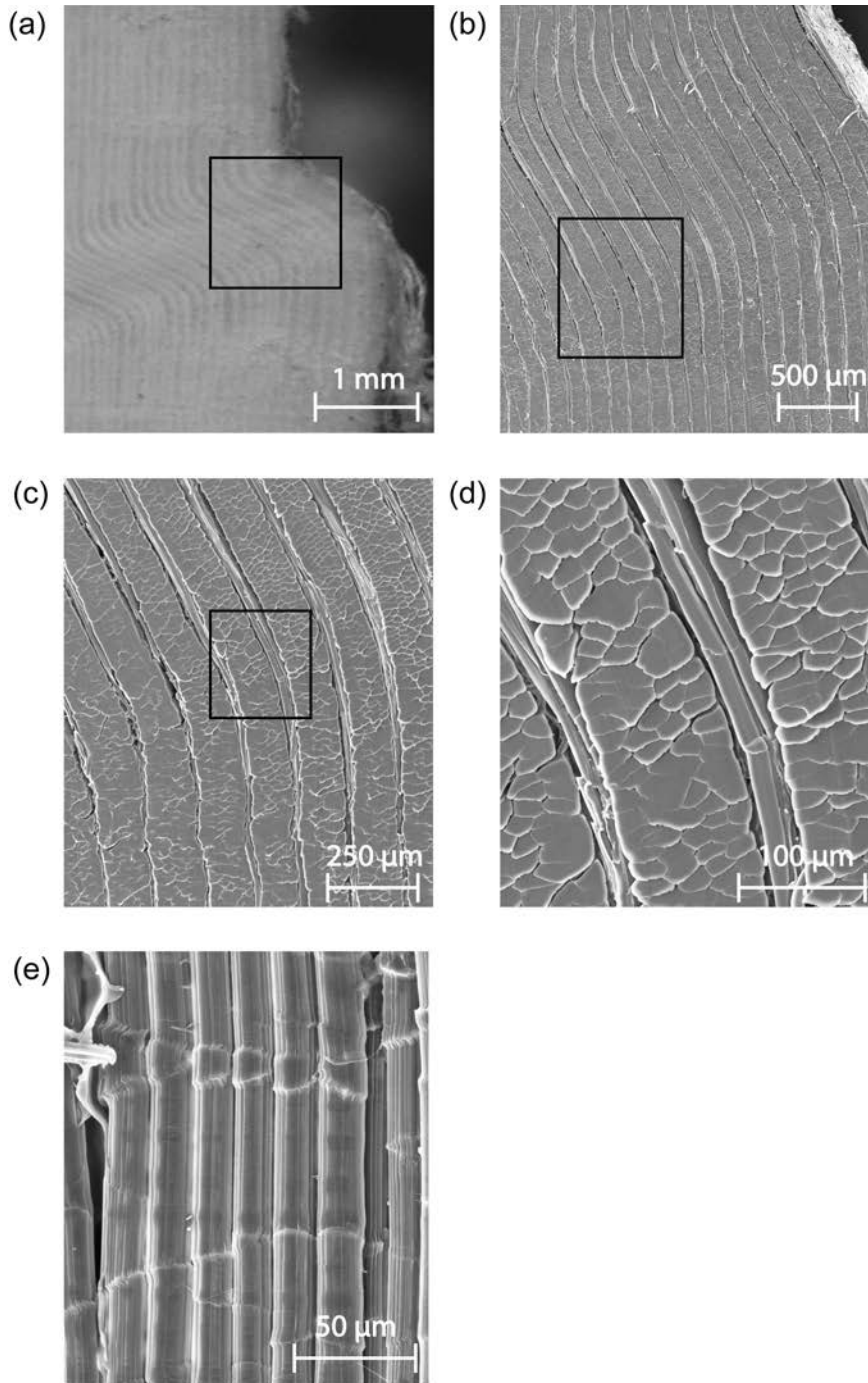


Figure 11: Images of the micro-buckle in the type A HB26 specimen edge (side view in Figure 7) at an applied displacement $u = 0.34$ mm at different levels of magnification. (a) Optical image showing an overall view. (b)-(d) SEM micrographs at different levels of magnification. The boxes in (a)-(d) show the section of the magnified view in the next image. (e) SEM micrographs of the fibre near the kink band edge showing the kinking of the fibres.

Considering the assumptions inherent in this simple analysis, Eq. (3.4) is sufficiently accurate for application in the HB26 composites with an SK76 fibre kinking strain $\varepsilon_c \approx 1\%$ as detailed in Section 2.2. Based on the measured values of E , τ_Y and t

detailed in Section 3.1, we estimate $w^* = 1.0$ mm which is in good agreement with the measurements from Fig. 9. This further confirms that micro-buckling here is occurring at the ply length scale rather than the fibre length scale (if micro-buckling was occurring due to shear between individual fibres, the Budiansky analysis would predict w^* to be about a factor of 4 smaller as each ply is approximately 4 fibre diameters thick). It is worth mentioning that w^* in most CFRP/GFRP composites is typically much smaller than that measured here for the HB26 composite for two reasons: (i) the shear strength of CFRP/GFRP composites is much higher with a typical value of $\tau_Y = 60$ MPa and (ii) the kink-band width in those composites scales with the fibre diameter while for HB26 it scales with the ply thickness that is nearly a factor of 6 larger than typical carbon fibre diameters.

The observations of Fig. 9 are quantified in Figs. 10c and 10d where we plot the measured misalignment angles $\bar{\phi} + \phi$ and band width w as a function of u . As described above, $\bar{\phi} + \phi$ initially increases until it reaches a critical value of $\approx 60^\circ$ beyond which it remains constant. Simple kinematics based on the assumptions of inextensible plies and no deformation outside the micro-buckle band gives an expression relating u and ϕ until the onset of band broadening as

$$u = w^*[\cos \bar{\phi} - \cos(\bar{\phi} + \phi)]. \quad (3.5)$$

Band broadening sets in after the rotation of the plies ceases. The kinematical description of kinking presented by Fleck & Budiansky (1990) suggests that the plies will rotate until the volumetric strain within the band vanishes and “lock-up” then occurs as the plies cannot rotate further without interpenetrating (assuming that the plies themselves are incompressible). This analysis gives the critical ply rotation $\phi_c = 2(\beta - \bar{\phi})$. Thus, the relation between ply rotation and compressive displacement is given by

$$\phi = \begin{cases} \cos^{-1} \left[\cos \bar{\phi} - \frac{u}{w^*} \right] - \bar{\phi} & \text{for } \phi \leq \phi_c \\ \phi_c & \text{otherwise.} \end{cases} \quad (3.6)$$

A plot of Eq. (3.6) with the measured value of $w^* = 0.96$ mm, $\bar{\phi} = 4^\circ$ and $\beta = 36^\circ$ is included in Fig. 10c and shows good agreement with the measurements. Similarly, the band width is related to u via the relation

$$w = \begin{cases} w^* & \text{for } u \leq u_c \\ \frac{uw^*}{u_c} & \text{otherwise,} \end{cases} \quad (3.7)$$

where $u_c = w^*[\cos \bar{\phi} - \cos(\bar{\phi} + \phi_c)]$ is the critical displacement at which band broadening commences. The prediction, Eq. (3.7), included in Fig. 10d is again in good agreement with the measurements.

3.3.2 Micro-buckle propagation versus applied stress

The initiation and propagation of a micro-buckle in CFRP composites has been modelled as a crack problem with a tip toughness and crack bridging stress associated with the micro-buckle; see Sivashanker et al. (1996) for further details. The

photographs in Fig. 8 and the σ versus Δa measurement for the type A specimen shown in Fig. 10b suggests that a similar analysis might also apply to Dyneema[®] composites. Toughness governed micro-buckle initiation requires that the peak stress σ_{\max} to scale with the specimen size. In particular specimen types A and B are geometrically self-similar with specimen B a factor of 3.3 smaller compared to specimen A and thus toughness governed micro-buckle initiation will suggest that σ_{\max} in specimen type B is a factor of $\sqrt{3.3}$ larger than that in specimen type A. We now proceed to report measurements on specimen type B to test this hypothesis.

The measured σ versus δ response of the HB26 composite using specimen type B is included in Fig. 10a while the corresponding $\sigma - \Delta a$ curve is plotted in Fig. 10b. The tests on the type B specimens were carried out in an identical manner to those on the type A specimen except that the applied displacement rate was also scaled by a factor of 3.3 so as to keep the applied nominal strain rate the same for both specimen types. These tests were again terminated when the out-of-plane displacement exceeded 10% of the specimen thickness. However, the smaller specimen thickness implied that this condition was attained at a smaller value of the applied displacement δ . In order to illustrate this drawback of thinner specimens, consider the case of deformation assuming inextensible fibres and no deformation occurring outside the micro-buckle band. We constrain the total out-of-plane displacement (including that due to the initial misalignment) to be $v = w \sin(\phi + \bar{\phi}) \leq fb$ where $0 < f \leq 1$ so as to limit the induced bending stresses. Using the Eq. (3.5) for the compressive displacement, the limiting compressive displacement u_e at which the $v = fb$ is found to be given by

$$u_e = \begin{cases} w^* \left[\cos \bar{\phi} - \sqrt{1 - \left(\frac{fb}{w^*}\right)^2} \right] & \text{for } \sin(\phi_c + \bar{\phi}) \geq \frac{fb}{w^*} \\ \frac{fb}{\sin(\phi_c + \bar{\phi})} [\cos \bar{\phi} - \cos(\bar{\phi} + \phi_c)] & \text{otherwise.} \end{cases} \quad (3.8)$$

In Eq. (3.8) the first branch represents the case when the critical displacement u_e is attained prior to the commencement of band broadening while the second represents the case when u_e is attained during the band broadening phase. For the HB26 composite with $\phi_c + \bar{\phi} \approx 60^\circ$ and $w^* \approx 1$ mm, u_e is attained in the band broadening phase for $b = 20$ mm (specimen type A) and prior to the commencement of band broadening for $b = 6$ mm (specimen type B) with an assumed value $f = 0.1$ (which is consistent with the criterion used to terminate the experiments). Thus, while some initial fibre rotation measurements for the type B HB26 composite are included in Fig. 10c we report no band broadening measurements for the type B specimen in Fig. 10d. It is noted in passing that in most CFRP/GFRP composite specimens, u_e is typically always attained in the band broadening phase. This is because w^* in those composites is much smaller compared to the Dyneema[®] composites for reasons discussed above.

The data in Fig. 10a shows that the micro-buckle initiation stress σ_{\max} is nearly independent of the specimen size suggesting that a toughness analysis cannot be used to describe micro-buckle initiation and propagation in the HB26 Dyneema[®] composites. In fact the process seems more likely to be stress controlled. To rationalise this, consider the problem sketched in Fig. 12a of a specimen with an edge crack: micro-buckling is assumed to occur in the crack plane when the compressive

stress attains a local value equal to the micro-buckling stress. In an elastic specimen, the crack introduces a stress singularity at the crack tip. However, if anisotropic plastic yielding occurs then there is significant stress redistribution. In particular, if the only non-zero plastic strain component was γ_{XY} then a plastic zone as shown in Fig. 12a forms and significantly relaxes the stresses ahead of the crack. This problem was analysed by Chan et al. (1993) in the context of layered materials. Denoting the shear strength τ_{XY} as τ_Y , we plot in Fig. 12b the variation of the normal stress σ_{YY} ahead of a crack tip (i.e. infinitely sharp notch) for three choices of σ/τ_Y where σ is the remote applied stress; see Chan et al. (1993) for details. Recall that a sharp crack was made in the notch roots of the specimens used in this study and thus the edge crack results are directly applicable to analyse the specimens tested. Micro-buckling is observed to initiate when $\sigma = \sigma_{\max} = 12$ MPa and thus the stress distribution ahead of the crack/notch at the initiation of micro-buckling is that for the case with $\sigma/\tau_Y = 6.4$ in Fig. 12b. (The shear strength of the HB26 composite $\tau_Y \approx 1.8$ MPa; see Appendix A.) The stress at the crack/notch root is approximately uniform across the net-section of the specimen and only about 40% higher than the remote applied stress at the notch root. Thus, micro-buckling initiates at the notch root and the remote applied micro-buckle initiation stress is reasonably specimen size independent as the stress field in the specimen is reasonably spatially uniform, i.e. micro-buckle initiation is net-section stress governed.

To understand the propagation Δa of the micro-buckle ahead of the notch root we first need to propose a relation for the compressive traction σ_c versus compressive displacement u of the material within the micro-buckled band. For simplicity we assume a relation of the type sketched in Fig. 12c with the micro-buckle initiating at $\sigma_c = \sigma_{\max}$ and the stress dropping to zero over a displacement $u = \Delta_n$, i.e. the micro-buckle band broadening stress σ_b is negligible. To rationalize this recall that $\sigma_b \approx 2G\gamma_Y = 2\tau_Y$ (Fleck 1997). However, the inter-laminar shear stress measurements included in Appendix A show that the shear strength of HB26 drops sharply to nearly zero after attaining its initial peak value of 1.8 MPa. Thus, we anticipate the shear stress to drop to nearly zero within a micro-buckle undergoing large deformations and thus $\sigma_b \approx 0$.

Now consider the propagation of the micro-buckle by an increment $\delta a \gg \Delta_n$. The plastic zone extends to the new crack tip as sketched in Fig. 12d and the distribution of the stress σ_{YY} on the crack plane is included schematically in an inset in Fig. 12d. Again, ahead of the new crack tip the stress field is given by the Chan et al. (1993) analysis with $\sigma/\tau_Y = 6.4$ and there exists a bridging zone behind this new crack tip of length $\approx \Delta_n$ before which the stress drops to zero. If Δ_n is small compared to the specimen dimensions then this bridging zone can be neglected and the applied $\sigma - \Delta a$ relation follows from a net-section analysis as

$$\sigma = \sigma_{\max} \left[1 - \frac{\Delta a}{(D - d)} \right]. \quad (3.9)$$

The predictions of Eq. (3.9) are included in Fig. 10b for both the type A and type B HB26 specimens and are in excellent agreement with the measurements.

In summary, the observations and analysis presented above suggest that conventional micro-buckling analysis suffices to predict the compressive strength of the HB26 composite with the following caveats: (i) micro-buckling occurs at a ply level due to shearing between plies rather than between individual fibres; (ii) the kink width is set by the compressive kinking strain of the fibres rather than the strain to cause tensile fracture of the fibres; (iii) the band broadening stress $\sigma_b \approx 0$ as matrix damage degrades the shear strength of the matrix within the micro-buckle very rapidly and (iv) the initiation and propagation of the micro-buckle is net-section stress rather than toughness governed.

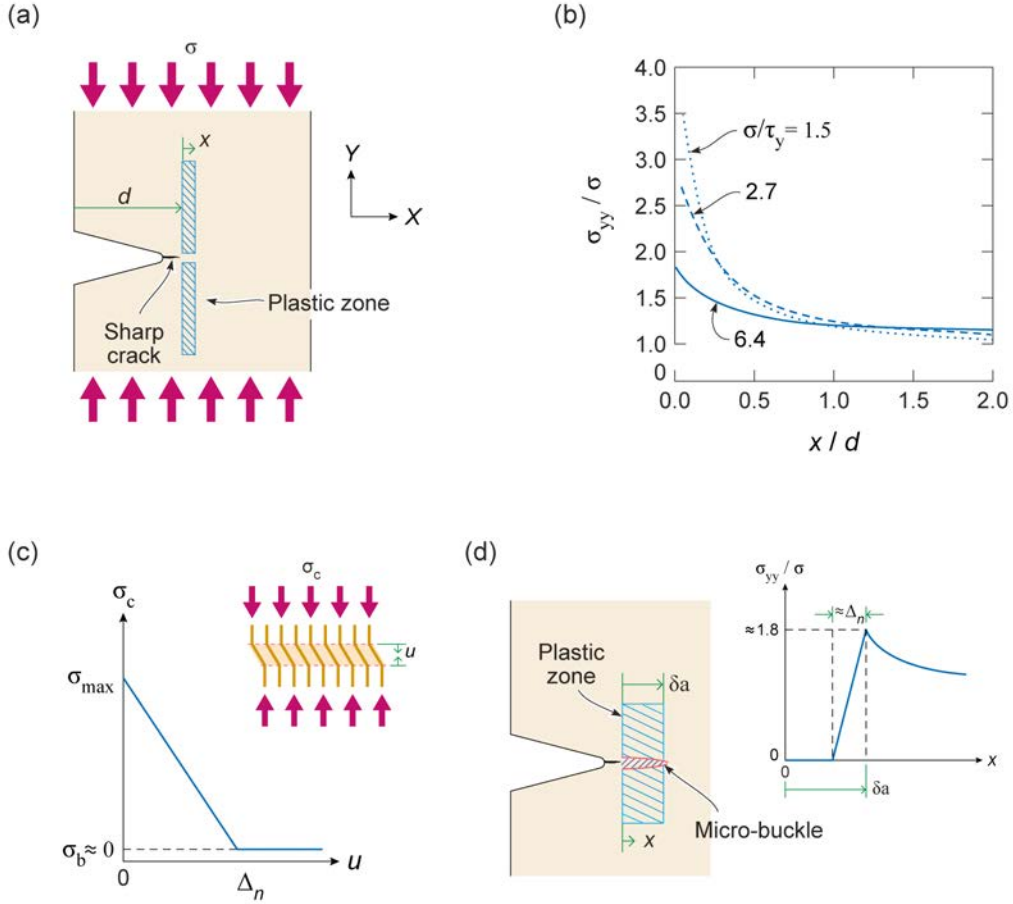


Figure 12: (a) Sketch of an edge-notched specimen (with a sharp crack at the root) subjected to a remote stress σ . The plastic zone emanating from the crack tip is illustrated. (b) Predictions of the distribution of the stress σ_{YY} ahead of the crack tip for three choices of the applied stress to shear strength ratio σ/τ_Y . (c) The assumed compressive traction σ_c versus compressive displacement u relation of the material within the micro-buckled band. (d) Sketch of the plastic zone after the micro-buckle has propagated a distance δa . The inset shows a sketch of the distribution of the stress σ_{YY} ahead and behind the tip of the propagated micro-buckle.

3.4 Comparison between the HB26 and HB50 composites

Plates of the HB50 composite were only available with a thickness $b = 6$ mm and thus compression specimens of the HB50 composite were manufactured using geometry type B.

The measured σ versus δ response of the HB50 composite using specimen type B was also included in Fig. 10a. While the initial elastic modulus of the HB50 specimen is similar to the HB26 specimen, the peak strength of the HB50 composite is

significantly lower at $\sigma_{\max} \approx 3$ MPa. SEM micro-graphs of the HB50 composite suggest that the initial ply misalignment angles are similar for both the HB26 and HB50 composites and its shear modulus is also about 60 MPa (Liu et al. 2013). However, the peak inter-laminar shear strength is much lower for the HB50 composite with $\tau_Y = 0.2$ MPa (Appendix A). Using these values in Eq. (3.1) the micro-buckling strength is estimated to be $\sigma_{mb} = 2.5$ MPa; in good agreement with the σ_{\max} measurement in Fig. 10a. Image analysis, similar to that detailed in Section 3.3 for the HB26 composite, confirmed that the HB50 micro-buckle initiation and propagation followed a similar sequence to the HB26 composite. In particular, a kink band with $\beta = 29^\circ$ and $w^* = 3$ mm was formed. Thus, using the criterion in Eq. (3.9) it is clear that u_e is attained prior to the onset of band broadening in the type B HB50 specimen. Moreover, u_e is smaller for the HB50 type B specimen compared to the type B HB26 specimen due to the larger value of w^* in the HB50 composite. Thus, the compression tests on the HB50 composite were terminated slightly before those on the type B HB26 specimens.

Measurements of $\sigma - \Delta a$, $\phi - u$ and $w - u$ for the HB50 composite (specimen type B) are included in Fig. 10b, 10c and 10d, respectively. The corresponding predictions using Eqs. (3.4), (3.6) and (3.7) are included in the figures with values of material parameters representative of HB50. There is, in general, good agreement with the measurements, with the main differences between the HB50 and HB26 composites being (i) the lower micro-buckling strength of the HB50 composite and (ii) the larger kink band width w^* of the HB50 composite. Both of these differences are due to the lower shear strength of the SISTC matrix in the HB50 composite compared to the PADP matrix in the HB26 composite.

4. Concluding remarks

The compressive strength of SK76 fibres was measured via recoil and knot (bend) tests. Compressive kinks associated with micro-buckling of the fibrils within the fibres were first observed at a compressive stress of about 340 MPa in the recoil tests. By contrast, kinks were observed in the knot tests at compressive strains of around 1% corresponding to a compressive stress of about 880 MPa (based on a fibre modulus $E_f = 82$ GPa). This is consistent with measurements for aramid fibres where bend tests also gave strength measurements typically 2-3 times greater than those obtained from direct compression tests.

The in-plane compressive response of two grades (HB26 and HB50) of Dyneema[®] composites comprising approximately 83% volume fraction SK76 fibres was measured using notched specimens. The HB26 composite has a shear strength of about 1.8 MPa while the HB50 composite has a lower shear strength of about 0.2 MPa. Micro-buckling of the composites occurs by kinking of the plies due to inter-laminar shear with the HB26 composite having the higher strength of 12 MPa due to its higher shear strength, while the HB50 composite has a compressive strength of about 3 MPa. Thus, unlike Kevlar composites, the compressive strength of Dyneema[®] composites is governed by their inter-laminar shear strength and ply waviness rather than the compressive crush strength of the fibres. Applications requiring a higher compressive strength might therefore be realized by use of stronger polymer matrices.

In the notched specimens the micro-buckle initiates at the notch root and propagates across the specimen face. A net-section stress analysis adequately captures the measured applied remote stress versus micro-buckle propagation response. The kink band formed by the micro-buckled plies is inclined at approximately $\beta = 36^\circ$ and 29° in the HB26 and HB50 composites, respectively and the lower shear strength of the HB50 composite results in a larger kink width for the HB50 composite compared to the HB26 composite. Initial compression occurs by the rotation of the plies within the band until the plies rotate by $\phi \approx 2\beta$ at which point lock-up occurs. Further compression then occurs by the broadening of the kink band with no further rotation of the plies. Kinking theory is shown to capture measurements with adequate fidelity.

The observations and analysis presented here suggest that conventional micro-buckling analysis as developed for CFRP composites suffices to predict the compressive strength of the HB26 and HB50 composites with the following caveats: (i) micro-buckling occurs at a ply level due to shearing between plies rather than between individual fibres; (ii) the kink width is set by the compressive kinking strain of the fibres rather than the strain to cause tensile fracture of the fibres (iii) the band broadening stress in these composites is negligible as matrix damage degrades the shear strength of the matrix within the micro-buckle very rapidly and (iv) the initiation and propagation of the micro-buckle is net-section stress rather than toughness governed.

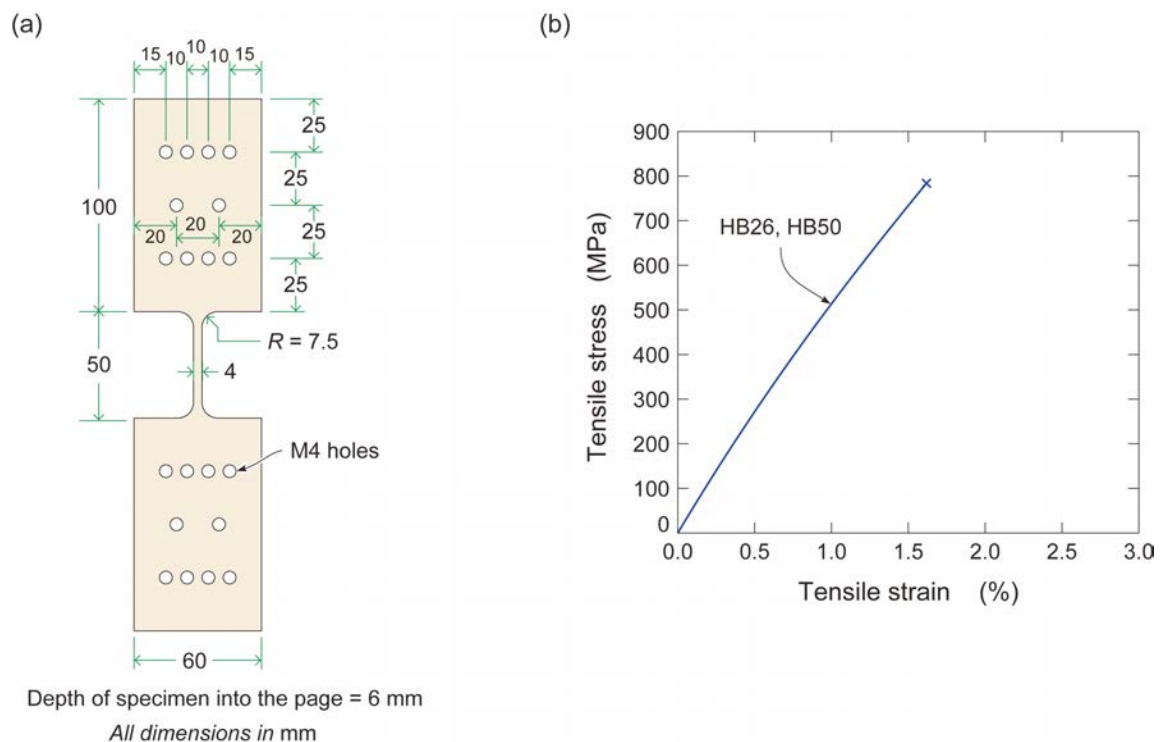


Figure A1: (a) Sketch of the front view of the tensile specimen. All leading dimensions marked in mm. (b) The measured tensile stress versus strain responses of the HB26 and HB50 composites (these are nearly indistinguishable).

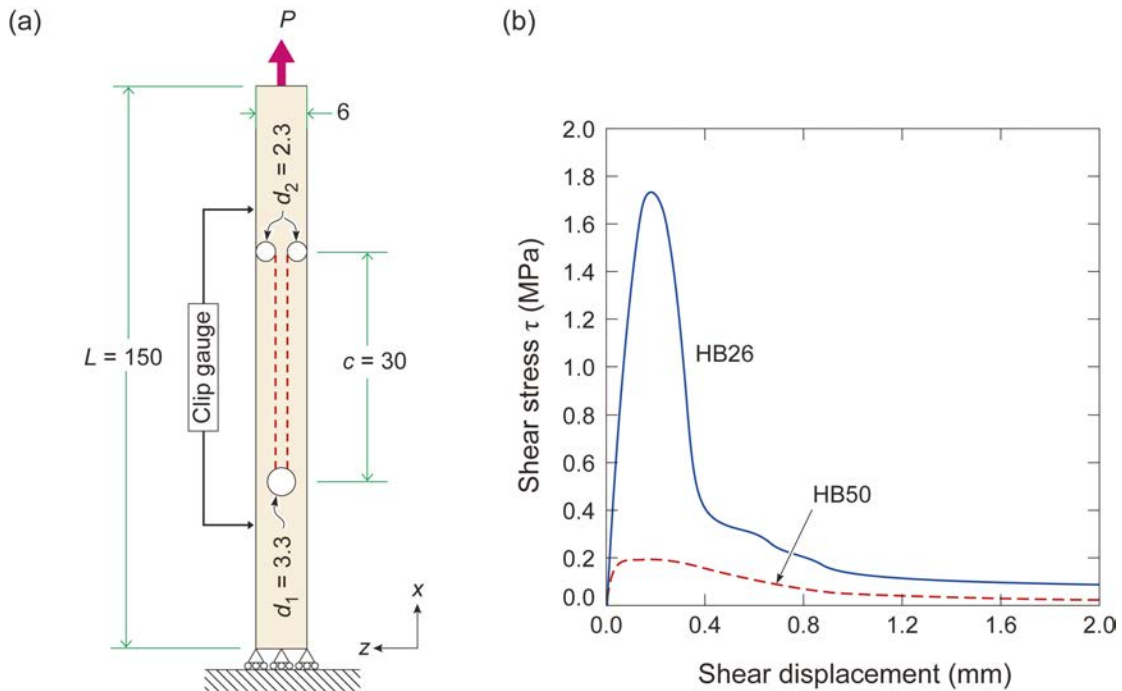
Appendix A: Measurements of the tensile and shear properties of the HB26 and HB50 composites

Two types of quasi-static material characterization tests were performed in order to measure the tensile and inter-laminar shear responses of the two grades of Dyneema®

composites:

(i) Uniaxial tensile tests in an orientation such that the 0° plies were aligned with the tensile axis. The Dyneema[®] composites have a high tensile strength along the fibre directions, but a very low shear strength. Thus, a standard tabbed tensile specimen cannot be used as discussed in (Russell et al. 2013). They employed a specimen with a large gripping area and a narrow gauge width as sketched in Fig. A1a. The tensile tests were conducted in a screw driven test machine at a nominal applied strain rate of 10^{-3}s^{-1} with the nominal stress determined by measuring the load from the load cell of the test machine. The axial nominal strain was measured using a clip gauge of gauge length 12.5 mm.

(ii) Double-notch shear tests (Liu et al. 2013) were used to measure the inter-laminar shear response, Fig. A2a. Specifically, strips of length 150 mm, width $b = 20$ mm and thickness 6 mm were cut from the Dyneema[®] composite sheets. Inter-laminar shear was promoted over a gauge length $c = 30$ mm by drilling three holes of diameters d_1 and d_2 over the central section of the specimen as sketched in Fig. A2a. Care was taken to ensure that the hole/notches were positioned such that there were no continuous fibres that spanned the entire length of the specimen. The tests were conducted by friction gripping the specimen ends and pulling them, as indicated in Fig. A2a in a screw driven test machine. The inter-laminar shear stress τ as defined as $\tau \equiv P/(2cb)$, where P is the measured tensile load and the factor of 2 is present as the shear force P is shared by 2 inter-laminar planes, as shown by the dashed lines in Fig. A2a. The shear displacements were measured by mounting a clip gauge on either side of the notch. These tests were conducted at an applied displacement rate of 1 mm/min.



Depth of specimen into the page, $b = 20$ mm
All dimensions in mm

Figure A2: (a) Sketch of the side view of the double-notch shear specimen. All leading dimensions marked in mm. (b) The measured shear stress τ versus shear displacement responses of the HB26 and HB50 composite.

The tensile stress versus strain curves of the HB26 and HB50 composites are plotted in Fig. A1b. Both grades display an approximately elastic-brittle tensile response with a tensile strength $\sigma_T \approx 800$ MPa as the behaviour is mainly governed by the SK76 fibres. The inter-laminar shear responses, as measured using the double-notch shear tests, are plotted in Fig. A2b. The peak shear strength of the HB26 matrix is around 1.8 MPa while the HB50 grade has a significantly lower strength of 0.2 MPa. The shear strength degrades sharply after the peak strength is attained.

Acknowledgements

This research was funded by the Defense Advanced Research Projects Agency (DARPA) under grant number W91CRB-11-1-0005 (Program manager, Dr. J. Goldwasser). We are grateful to DSM for the supply of the materials used in this study, and to Mr. Alan Heaver for his technical assistance in performing the recoil and knot tests.

References

- Allen, S.R., 1987. Tensile recoil measurement of compressive strength for polymeric high performance fibres. *Journal of Materials Science*, (22), pp.853–859.
- Attwood, J.P. et al., 2014. The out-of-plane compressive response of Dyneema composites. *Journal of the Mechanics and Physics of Solids*, 70, pp.200–226.
- Budiansky, B., 1983. Micromechanics. *Computers and Structures*, 16(1-4), pp.3–12.
- Chan, K.S., He, M.Y. & Hutchinson, J.W., 1993. Cracking and stress redistribution in ceramic layered composites. *Materials Science and Engineering: A*, 167, pp.57–64.
- Chocron Benloulou, I.S. et al., 1997. Dynamic tensile testing of aramid and polyethylene fibre composites. , 19(96), pp.135–146.
- Fleck, N.A., 1997. Compressive Failure of Fiber Composites. *Advances in Applied Mechanics*, 33, pp.43 – 113.
- Fleck, N.A. & Budiansky, B., 1990. Compressive Failure of Fibre Composites Due to Microbuckling. In *IUTAM Symposium*.
- Govaert, L.E. & Lenstra, P.J., 1992. Deformation behavior of oriented UHMWPE fibers. *Colloid and Polymer Science*, 270, pp.455–464.
- Greenwood, J.H. & Rose, P.G., 1974. Compressive behaviour of Kevlar 49 fibres and composites. *Journal of Materials Science*, 9, pp.1809–1814.
- Grujicic, M. et al., 2009. Multi-scale ballistic material modeling of cross-plyed compliant composites. *Composites Part B: Engineering*, 40(6), pp.468–482.

- Iannucci, L. & Pope, D., 2011. High velocity impact and armour design. *Express Polymer Letters*, 5(3), pp.262–272.
- Jones, W.R. & Johnson, J.W., 1971. Intrinsic Strength and Non-Hookean Behaviour of Carbon Fibres. *Carbon*, 9, pp.645–655.
- Koh, A.C.P., Shim, V.P.W. & Tan, V.B.C., 2010. Dynamic behaviour of UHMWPE yarns and addressing impedance mismatch effects of specimen clamps. *International Journal of Impact Engineering*, 37(3), pp.324–332.
- Kyriakides, S. & Ruff, A.E., 1997. Aspects of the Failure and Postfailure of Fiber Composites in Compression. *Journal of Composite Materials*, 31(16), pp.1633–1670.
- Liu, G. et al., 2013. Collapse of a composite beam made from ultra high molecular-weight polyethylene fibres. *Journal of the Mechanics and Physics of Solids*, pp.1–16.
- O'Masta, M.R., Deshpande, V.S. & Wadley, H.N.G., 2015. Defect controlled transverse compressive strength of polyethylene fiber laminates. *International Journal of Solids and Structures*, 52, pp.130–149.
- O'Masta, M.R., Deshpande, V.S. & Wadley, H.N.G., 2014. Mechanisms of projectile penetration in Dyneema encapsulated aluminum structures. *International Journal of Impact Engineering*, 74, pp.16–35.
- Piggott, M.R. & Wilde, P., 1980. Compressive strength of aligned steel reinforced epoxy resin. *Journal of Materials Science*, 15, pp.2811–2815.
- Russell, B.P. et al., 2013. The high strain rate response of Ultra High Molecular-weight Polyethylene: From fibre to laminate. *International Journal of Impact Engineering*, 60, pp.1–9.
- Sivashanker, S., Fleck, N.A. & Sutcliffe, M.P.F., 1996. Microbuckle Propagation in a Unidirectional Carbon Fibre-Epoxy Matrix Composite. *Acta Materialis*, 44(7), pp.2581–2590.
- Vogler, T. & Kyriakides, S., 1997. Initiation and axial propagation of kink bands in fiber composites. *Acta Materialia*, 45(6), pp.2443–2454.
- Wilding, M.A. & Ward, I.M., 1978. Tensile creep and recovery in ultra-high modulus linear polyethylenes. *Polymer*, 19, pp.969–976.